Frictionally Induced Asymmetries in Wind-Driven Flows

JANINE J. NAUW AND HENK A. DIJKSTRA[*]

Institute for Marine and Atmospheric Research Utrecht, Department of Physics and Astronomy, Utrecht University, Utrecht, Netherlands

ERIC P. CHASSIGNET

Rosenstiel School of Marine and Atmospheric Science, University of Miami, Miami, Florida

ABSTRACT

The effect of the parameterization of lateral friction on the separation of western boundary currents is addressed in an idealized context. The study is motivated by a puzzling issue that arises from the nonlinear theory of the wind-driven double-gyre circulation in shallow-water models. Subtle changes in the representation of the lateral friction in these models have a substantial effect on both steady-state and transient flows. The aim of this paper is to explain how lateral friction introduces a north–south asymmetry in the steady double-gyre flows and why the degree of this asymmetry depends on the type of frictional parameterization. A more conceptual model of a zonal jet in a channel turns out to be very useful to determine the dynamical processes behind the asymmetries. It is also shown that the north–south asymmetries have an impact on the low-frequency variability of the time-dependent flows. This is caused by changes in stability behavior of the steady-state flows.

1. Introduction

The theory of the wind-driven ocean circulation, as initiated by Sverdrup, Stommel, and Munk, is one of the cornerstones of dynamical oceanography (Sverdrup 1947; Stommel 1948; Munk 1950). These early linear theories were aimed at explaining qualitative properties of ocean flows, such as the east–west asymmetry and the presence of boundary currents. In the following decades, nonlinear aspects of these flows, such as the introduction of north–south asymmetry through inertia and the effect of instabilities, have been considered extensively (Pedlosky 1996). At the present time, many numerical models of the ocean circulation have been developed. Highly transient flows are simulated with properties much like those of the observed circulation using high-resolution ocean models (Smith et al., 2000; Hurlburt and Hogan 2000; Chassignet and Garraffo 2001). However, there still appears to be quite a gap in the understanding of these complex flows through a systematic extension of the theory of the wind-driven circulation (McWilliams 1996; Pedlosky 1996).

Recently, progress has been made in bridging this gap by using dynamical systems methods. The approach is to monitor the transitions, or successive bifurcations, of wind-driven flows as parameters are changed from weakly to strongly forced regimes. One of the systems extensively studied is the double-gyre circulation in a rectangular domain. The bifurcation structures of these flows have been clarified now in both quasigeostrophic and shallow-water models. When forcing is increased (or friction decreased), there is a transition from a unique steady state regime through a multiple steady-state regime (Cessi and Ierley 1995; Dijkstra and Katsman 1997), local oscillatory instabilities (Simonnet and Dijkstra 2002), and global bifurcations to very complex transient behavior (Nadiga and Luce 2001).

In shallow-water models of the double-gyre circulation, the flow within each layer is represented by the horizontal velocity field $\mathbf{u} = (u, v)$ and the layer thickness field h. Dissipation in the large-scale ocean circulation occurs by turbulent processes over an enormous range of scales, many of which cannot be represented in these models. The effects of these unresolved scales are usually represented by an eddy viscosity parameterization, which causes downgradient transport. However, there is a choice to parameterize the lateral (eddy) momentum friction, which will be denoted by the two-dimensional vector function $\mathcal{F}$ in the rest of this paper. With A_H indicating a constant eddy-diffusivity, the following forms have appeared in the literature:

* Current affiliation: Department of Atmospheric Science, Colorado State University, Fort Collins, Colorado.

Corresponding author address: Dr. Janine J. Nauw, Institute for Marine and Atmospheric Research Utrecht, Department of Physics and Astronomy, Utrecht University, Princetonplein 5, 3584 CC Utrecht, Netherlands.
E-mail: j.j.nauw@phys.uu.nl
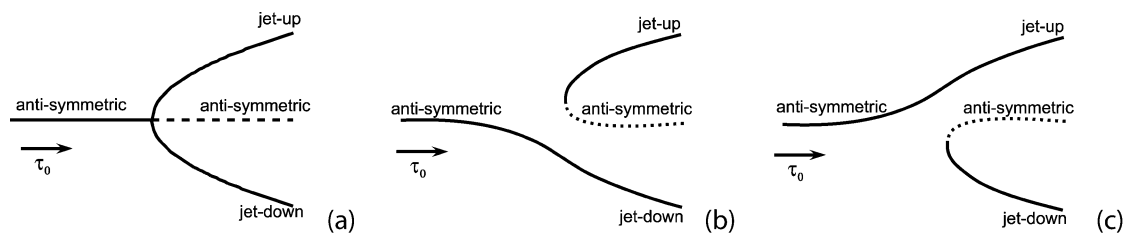
FIG. 1. Schematic figures of the typical bifurcation structure of the double-gyre wind-driven circulation. On the horizontal axis is the amplitude of the wind stress forcing τ_0, and on the vertical axis is the northward displacement of the jet w.r.t. the center of the basin. Solid (dashed) lines represent (un)stable steady states. Schematic bifurcation diagram (a) for quasigeostrophic models, (b) for shallow-water models with $\mathcal{F}_M$, and (c) for shallow-water models with $\mathcal{F}_F$.

1) The Laplacian form (Holland and Lin 1975), given by

$$\mathcal{F}_M = A_H \nabla^2 \mathbf{u}, \qquad (1)$$

arises by assuming that the horizontal velocities are constant over a layer (Dijkstra and Molemaker 1999; Nauw and Dijkstra 2001).

2) Another form of the lateral friction is given by

$$\mathcal{F}_E = \frac{A_H}{h} \nabla \cdot (h \nabla \mathbf{u}). \qquad (2)$$

In Gent (1993) it is shown that, for this form of momentum dissipation, it can be proven that the basin-integrated viscous dissipation is negative definite.

3) A third form is given by

$$\mathcal{F}_F = \frac{A_H}{h} \nabla^2 (\mathbf{u}h). \qquad (3)$$

This is used when the shallow-water equations are written in flux formulation (Speich et al. 1995; Jiang et al. 1995).

One of the limits of the shallow-water theory is the quasigeostrophic theory (Pedlosky 1987) in which the two forms of lateral friction $\mathcal{F}_E$ and $\mathcal{F}_F$ reduce to $\mathcal{F}_M$. For the double-gyre problem, the quasigeostrophic model is invariant to a north–south reflection with respect to the midaxis of the basin. When the steady states of this model are considered versus A_H, a branch with antisymmetric solutions is found. At some value of A_H, these solutions destabilize through a symmetry-breaking pitchfork bifurcation (Fig. 1a). The latter introduces two new branches with asymmetric steady states. One of these is characterized by solutions with the jet separating south of the zero wind stress curl line (ZWCL) and having a southwestward direction (''jet-down'' solutions); the other one is directly related by the reflection through the midaxis and consists of ''jet-up'' solutions.

When the branches of steady states of the double-gyre wind-driven circulation are considered versus the strength of the forcing (or friction) in shallow-water models, subtle qualitative differences arise in the bifurcation structure when using the different forms $\mathcal{F}_M$ and $\mathcal{F}_F$. For both cases, the reflection symmetry is absent

and consequently an imperfect pitchfork bifurcation results (Figs. 1b,c). For the form $\mathcal{F}_M$, the branch with jet-down solutions is connected to the one with nearly antisymmetric solutions (Fig. 1b). At high forcing, an isolated branch is created that consists of asymmetric jet-up and unstable nearly antisymmetric solutions [e.g., Fig. 5 in Dijkstra and Molemaker (1999) and Fig. 1 in Nauw and Dijkstra (2001)]. A qualitatively different bifurcation diagram is found for the form $\mathcal{F}_F$. The topological structure (Fig. 1c) of the branches is the mirror image of the one obtained for the form $\mathcal{F}_M$ [see also Fig. 1 in Speich et al. (1995) and Fig. 3 in Jiang et al. (1995)].

At first, this may seem to be an unimportant detail. However, the bifurcation diagrams computed for shallow-water models in basins with realistic continental boundaries are similar to those for rectangular basins, with the same imperfect pitchfork as in Figs. 1b and 1c. In these more realistic basins, the stable jet-up and jet-down solutions ''deform'' into two different separation patterns of the Gulf Stream and of the Kuroshio (Dijkstra and Molemaker 1999; Schmeits and Dijkstra 2000, 2001). The effect of the parameterization of the friction on the separation dynamics of the Gulf Stream is recognized in many ocean models (Böning and Budich 1992; Chassignet and Gent 1991; Hurlburt and Hogan 2000; Chassignet and Garraffo 2001), but it is not very well understood. It is therefore of interest to further investigate the impact of the representation of lateral friction on separation dynamics in the idealized rectangular basin case.

Chassignet and Gent (1991) have shown that the separation behavior is different in level models and layer models. The formulation of the wind stress forcing turns out to be crucial since it acts as a body force on the uppermost level or layer. In level models the acceleration due to the wind stress forcing is equally strong in the subtropical and subpolar gyre, while in layer models it is layer-thickness dependent. In layer models the curl of the wind stress is divided by the ''actual'' upper-layer thickness h instead of by the constant upper-level thickness H_0, which is used in level models. Hence, in layer models the Sverdrup solution becomes asymmetric with respect to the ZWCL, with larger velocities in the subpolar than in the subtropical gyre. Chassignet and Gent (1991) explain the preference for a jet-down solution in

layer models by assuming that a surface intensified sub-polar gyre is related to a southward overshoot of the subpolar western boundary current and a midlatitude jet separation south of the ZWCL. Moreover, in Cessi (1991) it was demonstrated that two colliding boundary currents with a larger transport in the northward-flowing boundary current results in a separation south of the ZWCL.

In this paper, we address the issue of asymmetry in shallow-water models by investigating the role of the different formulations of lateral friction. In addition to the bifurcation diagrams computed for $\mathcal{F}_F$ in Speich et al. (1995) and for $\mathcal{F}_M$ in Dijkstra and Molemaker (1999), we will here show the one for $\mathcal{F}_E$. Next, we focus in detail on the differences in the steady states and their stability between the cases $\mathcal{F}_M$ and $\mathcal{F}_E$. The bifurcation diagrams reveal that differences between the steady-state solutions occur already in the weak forcing limit, just before the emergence of multiple equilibria. The effect of the parameterization of the friction will be discussed with help of a conceptual model of a zonal jet in a channel. Additionally, the influence of inertia, which is responsible for the presence of multiple equilibria, is investigated. Moreover, the impact of the different parameterization of the friction on the time-dependent flows at higher forcing and in particular on their low-frequency variability is addressed.

2. The 1.5-layer shallow-water model

The reduced-gravity, shallow-water model captures the most relevant aspects of the wind-driven circulation within one layer of fluid with constant density ρ overlying an infinitely deep (or motionless) layer with density $\rho + \Delta\rho$. The layer thickness is indicated by $h(x, y, t)$ with an equilibrium (no flow) value of H_0. We consider the flow in a rectangular basin with horizontal dimensions of 1000×2000 km^2 located on a β plane centered at 45°N. The flow is driven by a stationary zonal wind stress pattern $\boldsymbol{\tau} = (\tau^x, 0)$:

$$\frac{\partial u}{\partial t} + u\frac{\partial u}{\partial x} + v\frac{\partial u}{\partial y} - (f_0 + \beta_0 y)v = -g'\frac{\partial h}{\partial x} + A_H\mathcal{F}^x(u, h) + \frac{\tau^x}{\rho_0 h}, \tag{4a}$$

$$\frac{\partial v}{\partial t} + u\frac{\partial v}{\partial x} + v\frac{\partial v}{\partial y} + (f_0 + \beta_0 y)u = -g'\frac{\partial h}{\partial y} + A_H\mathcal{F}^y(v, h), \quad \text{and} \tag{4b}$$

$$\frac{\partial h}{\partial t} + \frac{\partial(uh)}{\partial x} + \frac{\partial(vh)}{\partial y} = 0, \tag{4c}$$

where f_0 is the Coriolis parameter at 45°N and β_0 is the local meridional derivative of the Coriolis parameter f. The reduced gravity is defined by $g' = \Delta\rho g/\rho$ and, as mentioned above, A_H is the (constant) lateral friction coefficient. The frictional terms $\mathcal{F}(\mathbf{u}, h)$ in (4) are parameterized as shown in the introduction, with $\mathcal{F}_M(\mathbf{u}, h) = \nabla^2\mathbf{u}$, $\mathcal{F}_E(\mathbf{u}, h) = h^{-1}\nabla\cdot(h\nabla\mathbf{u})$, and $\mathcal{F}_F(\mathbf{u}, h) = h^{-1}\nabla^2(\mathbf{u}h)$. On the lateral boundaries, no-slip conditions are prescribed. In all computations discussed below, the flow is forced by an idealized double-gyre wind stress with amplitude τ_0 and pattern

$$\tau^x(y) = -\tau_0 \cos\left(\frac{2\pi y}{B}\right), \tag{5}$$

where $B = 2000$ km is the meridional extent of the basin.

The governing equations and boundary conditions are discretized on a staggered Arakawa-C grid using second-order central differences, similar to the methodology in Speich et al. (1995); the horizontal resolution in all of the computations is 20 km. Bifurcation diagrams are computed by solving directly for the steady-state equations using continuation methods (Dijkstra 2000). For each steady state, the linear stability is determined by solving the corresponding generalized eigenvalue problem. Furthermore, time-dependent flows are calculated by integrating the equations forward in time. This is done with the equivalent barotropic version of the numerical model, described in Nauw and Dijkstra (2001), that uses also central differences but has an explicit time-marching scheme. The standard values of parameters used in the computations are shown in Table 1.

3. Results

In section 3a, we compare the bifurcation behavior of two different frictional representations by calculating steady-state solutions and their stability. In section 3b, it is shown that the differences in bifurcation structure have consequences for the steady-state behavior at low wind stress forcing. Furthermore, it is also shown that these parameterizations have an influence on the low-

TABLE 1. Standard dimensional parameters.

f_0	1.0×10^{-4} s^{-1}	H_0	7.0×10^2 m
β_0	2.0×10^{-11} (m s)$^{-1}$	A_H	3.0×10^2 m^2 s^{-1}
g'	2.0×10^{-2} m s^{-2}	τ_0	1.0×10^{-1} Pa
ρ_0	1.0×10^3 kg m^{-3}	B	2.0×10^6 m

frequency variability of the flow at high wind stress forcing (section 3c). In section 3d a simple conceptual model is used to gain insight into the frictionally induced asymmetries of the flows.

a. Bifurcation behavior

The bifurcation structure and the stability of the steady states are calculated for the model with parameterizations $\mathcal{F}_M$ and $\mathcal{F}_E$. The bifurcation behavior for $\mathcal{F}_F$ has already been calculated in Speich et al. (1995), although for somewhat different values of the parameters. However, they performed sensitivity analyses with several different control parameters, which all gave qualitatively similar results.

The bifurcation diagram for the case $\mathcal{F}_M$ is plotted in Fig. 2a. The amplitude of the wind stress τ_0 is used as a control parameter, while the minimum of the layer thickness h_{min} is used as a norm of the solution. The drawn curves represent linearly stable steady states, whereas the steady states represented by the dashed curves are unstable. The structure of this bifurcation diagram is as in the sketch of Fig. 1b with the jet-down branch at high forcing connected to the stable nearly "antisymmetric" branch at low forcing. Moreover, the jet-up and unstable nearly antisymmetric branch form an isolated branch. Note that the branches are named after the structure of the steady-state solutions. For the sake of brevity, the adverb "nearly," when we refer to the nearly antisymmetric steady states, will be suppressed in the rest of the paper.

The steady-state branches are exactly the same as those calculated for the two-layer shallow-water model in a previous study [see Fig. 1 in Nauw and Dijkstra (2001)]. This is because steady-state solutions in two-layer models without interfacial friction have a motionless lower layer; the latter is not directly forced. Steady states of such two-layer models therefore reduce to those of a 1.5-layer model. However, there is a difference in their stability behavior because the states in a two-layer model are susceptible to baroclinic instabilities.

Although the solutions in the bifurcation diagram for the parameterization $\mathcal{F}_E$ (Fig. 2b) appear similar to those of $\mathcal{F}_M$ in the low and high forcing regime, there is a different connection of the branches at intermediate values of the amplitude of the wind stress (between $6.0 \times 10^{-2} < \tau_0 < 9.0 \times 10^{-2}$ Pa). Note that the intersection between the jet-up branch and the unstable antisymmetric branch at $\tau_0 = 7.5 \times 10^{-2}$ Pa is not a connection between both branches but a consequence of the use of h_{min} as the norm of the solution. If the northward displacement of the jet with respect to the midaxis of the basin has been used as a norm of the solution, the bifurcation structure would be similar to the sketch in Fig. 1c.

By plotting the steady-state solutions for both cases in one diagram (Fig. 2c), the subtle effect of the frictional parameterization can be clearly seen. In the case
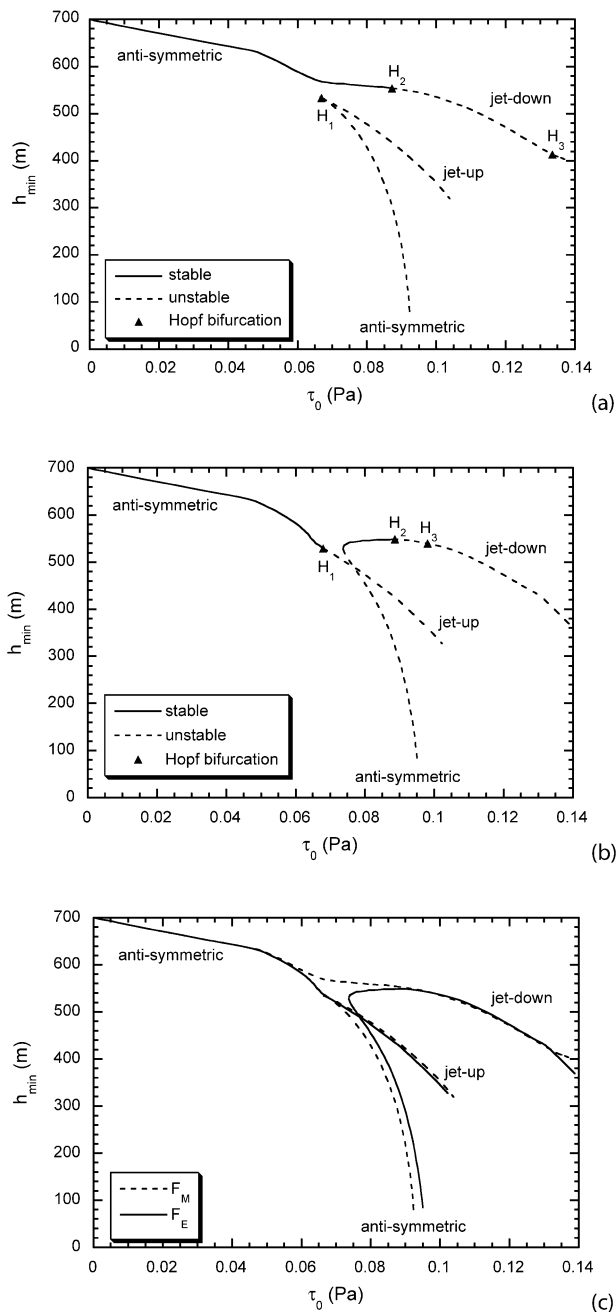
FIG. 2. Bifurcation diagrams of the steady-state solutions of the 1.5-layer shallow-water model. To monitor the solutions the minimum layer thickness h_{min} is plotted vs the wind stress strength τ_0. Solid (dashed) lines indicate stable (unstable) steady states and the filled triangles indicate Hopf bifurcations. The results of the model (a) with $\mathcal{F}_M$ and (b) with $\mathcal{F}_E$. (c) Both diagrams are repeated: the solutions with $\mathcal{F}_E$ ($\mathcal{F}_M$) are solid (dashed).

$\mathcal{F}_E$, the stable antisymmetric branch is connected to the jet-up branch instead of the jet-down branch, as is the case $\mathcal{F}_M$. Furthermore, the isolated branch is now formed by the unstable antisymmetric and the jet-down branch. The bifurcation diagram for the case $\mathcal{F}_F$, (Speich et al. 1995) is qualitatively similar to that of $\mathcal{F}_E$.

TABLE 2. (a) Values of the amplitude of the wind stress τ_0 (Pa), at which modes destabilize the steady states in Fig. 2. (b) Oscillation periods $\mathcal{P}$ (yr) of these modes at the Hopf bifurcations. Results are shown for the parameterizations $\mathcal{F}_M$ and $\mathcal{F}_E$.

Hopf bifurcation	$\mathcal{F}_M$	$\mathcal{F}_E$
	(a)	
H_1	6.7×10^{-2}	6.8×10^{-2}
H_2	8.7×10^{-2}	8.9×10^{-2}
H_3	1.3×10^{-1}	9.8×10^{-2}
	(b)	
H_1	34.7	17.7
H_2	1.8	1.8
H_3	9.4	10.8

The stability of the steady states has been calculated for both parameterizations and at each Hopf bifurcation (labeled with an H in Figs. 2a,b), a complex conjugate pair of eigenvalues $\sigma = \sigma_r \pm i\sigma_i$ crosses the imaginary axis. The corresponding eigenvectors $\mathbf{x} = \mathbf{x}_R \pm i\mathbf{x}_I$ provide the spatial pattern of the mode which destabilizes the steady state. The time-dependent behavior of this mode $\mathbf{P}(t)$, locally near the Hopf bifurcation, is given by

$$\mathbf{P}(t) = e^{\sigma_r t}[\mathbf{x}_R \cos(\sigma_i t) - \mathbf{x}_I \sin(\sigma_i t)], \qquad (6)$$

with angular frequency σ_i and growth rate σ_r; the oscillation period is given by $\mathcal{P} = 2\pi/\sigma_i$. The propagation of these modes can be followed by looking at the patterns $\mathbf{P}(-\pi/2\sigma_i) = \mathbf{x}_I$ and then at $\mathbf{P}(0) = \mathbf{x}_R$, which are one-quarter of a period apart. The locations of the Hopf bifurcations H_1, H_2, and H_3 and the oscillations periods are presented in Table 2 for both parameterizations $\mathcal{F}_M$ and $\mathcal{F}_E$.

The pattern of the steady-state layer thickness at the Hopf bifurcation H_1 for the case $\mathcal{F}_E$ (Fig. 2b) corre-

sponds to an asymmetric jet-up solution (Fig. 3a). The oscillation period of the mode destabilizing this state at H_1 has a period $\mathcal{P}_1 = 17.7$ yr. The imaginary and the real part of the perturbation layer thickness of the oscillatory mode are shown in Figs. 3b and 3c, respectively. They display the characteristic shifting of the jet in one phase and the strengthening or weakening in the other, which are characteristic for a gyre mode (Nauw and Dijkstra 2001; Simonnet and Dijkstra 2002). For values of τ_0 slightly above the Hopf bifurcation H_1, a periodic orbit associated with this gyre mode is expected.

For the case $\mathcal{F}_M$, the value of τ_0 of the Hopf bifurcation H_1 is near that for $\mathcal{F}_E$, but it is now located on the isolated branch (with jet-up solutions) near the saddle-node bifurcation. The latter is the reason for the longer period (34.7 yr) of the oscillatory mode which destabilizes the jet-up state for $\mathcal{F}_M$. The pattern of this mode is similar to that in Figs. 3b and 3c and hence is not shown.

The Hopf bifurcations H_2 occur at nearly the same position for both parameterizations of the friction (Figs. 2a,b), and in both cases an oscillatory mode with a period $\mathcal{P} = 1.8$ yr destabilizes the steady state. For the case $\mathcal{F}_M$, the steady-state layer thickness at the second Hopf bifurcation, H_2, clearly shows a jet-down solution (Fig. 4). The largest amplitudes of imaginary and real part of the perturbation layer thickness of the neutral mode (Figs. 4b,c) are located in the subpolar gyre. The pattern of this mode deforms into basinwide westward-propagating anomalies resembling inviscid Rossby basin modes (Pedlosky 1987), when it is continuously followed from Hopf bifurcation, H_2, along the jet-down branch until the amplitude of the wind stress becomes zero (not shown). Its interannual period, $\mathcal{P}_2 = 1.8$ yr is larger than the semiannual periods of Rossby basin

(a)   (b)   (c)
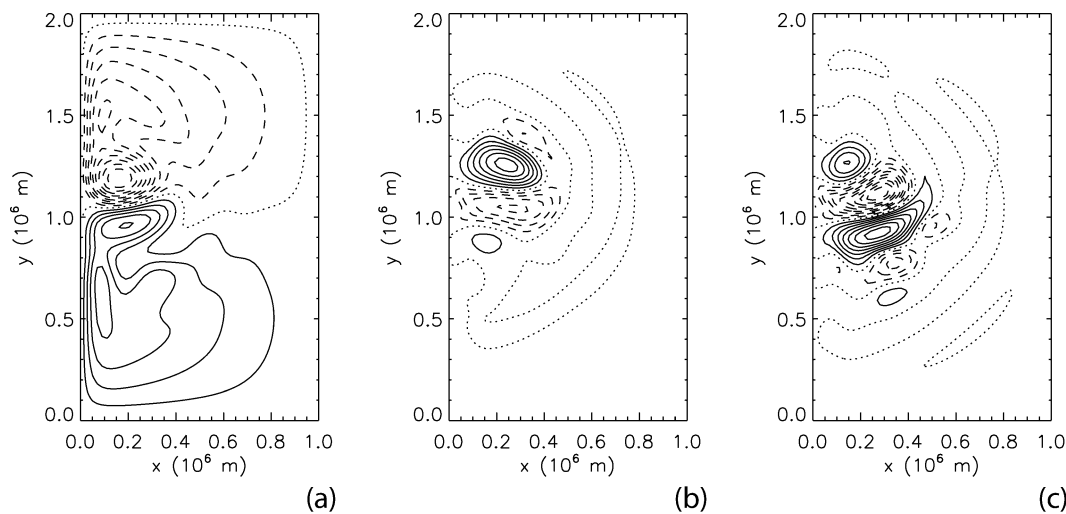
FIG. 3. (a) The layer thickness h of the steady state at Hopf bifurcation H_1 at $\tau_0 = 6.8 \times 10^{-2}$ Pa in the model with $\mathcal{F}_E$ and the (b) imaginary and (c) real perturbation layer thickness of the mode, which destabilizes at this Hopf bifurcation. The mode has a period of $\mathcal{P}_1 = 17.7$ yr.
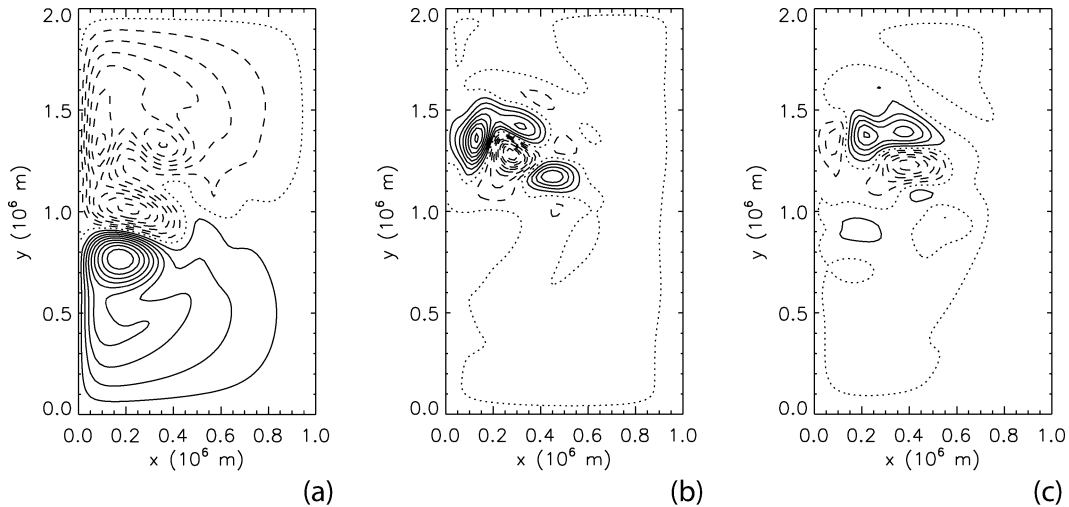
FIG. 4. As in Fig. 3 but for H_2 at $\tau_0 = 8.7 \times 10^{-2}$ Pa in the model with $\mathcal{F}_M$. The mode has a period of $\mathcal{P}_2 = 1.8$ yr.

modes found in previous studies (Speich et al. 1995; Dijkstra and Molemaker 1999). This can be attributed to the different values used for the Coriolis parameter, f_0. Here, we use $f_0 = 1.0 \times 10^{-4}$ s^{-1}, which represents a basin located at 45°N, while they use a value of $f_0 = 5.0 \times 10^{-5}$ s^{-1}, which shifts the basin to 21°N. This influences the internal Rossby radius of deformation and thereby the Rossby wave speed.

The frictional parameterization has not only an effect on the steady-state structure but also on the stability of these states. This is clearly seen by the large difference in the positions of the Hopf bifurcations H_3 (Figs. 2a,b). For $\mathcal{F}_E$, the jet-down state destabilizes at $\tau_0 = 9.8 \times 10^{-2}$ Pa while for $\mathcal{F}_M$ a substantially larger forcing $\tau_0 = 1.3 \times 10^{-1}$ Pa is needed. The steady-state layer thicknesses at H_3 are shown in Figs. 5a and 6a for the parameterization $\mathcal{F}_M$ and $\mathcal{F}_E$, respectively. Both are jet-down solutions, but the flow with $\mathcal{F}_M$, is somewhat stronger because of the larger forcing.

The imaginary and real part of the perturbation layer thickness of both neutral modes are shown in Figs. 5b and 6b and Figs. 5c and 6c, respectively. The pattern of the oscillatory mode for the case $\mathcal{F}_E$ clearly shows the characteristic strengthening of the jet during the phase of Fig. 6b, while it shifts the jet southward during the phase of Fig. 6c. Hence, this mode is an oscillatory gyre mode, which is also confirmed by its decadal period, $\mathcal{P}_3 = 10.8$ yr (Nauw and Dijkstra 2001).

The period of the third oscillatory mode for $\mathcal{F}_M$ is $\mathcal{P}_3 = 9.3$ yr, which is in the same range as that of the gyre mode. However, the oscillation pattern (Figs. 5b,c) only has a small resemblance to that of the gyre mode. There is only a small signature of the gyre mode in the imaginary part of the eigenvector (Fig. 5b) near the separated
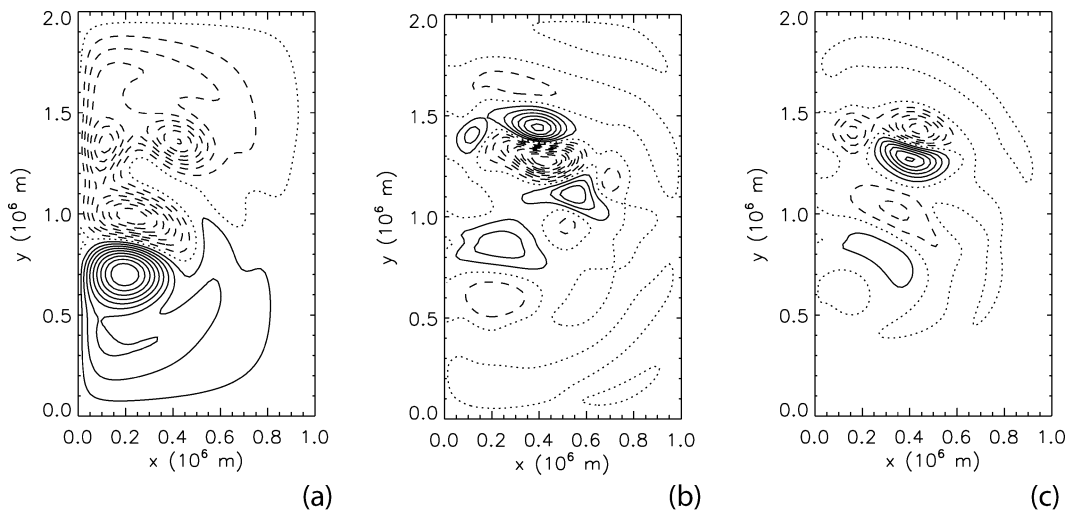
FIG. 5. As in Fig. 3 but for H_3 at $\tau_0 = 1.3 \times 10^{-1}$ Pa in the model with $\mathcal{F}_M$. The mode has a period of $\mathcal{P}_3 = 9.3$ yr.
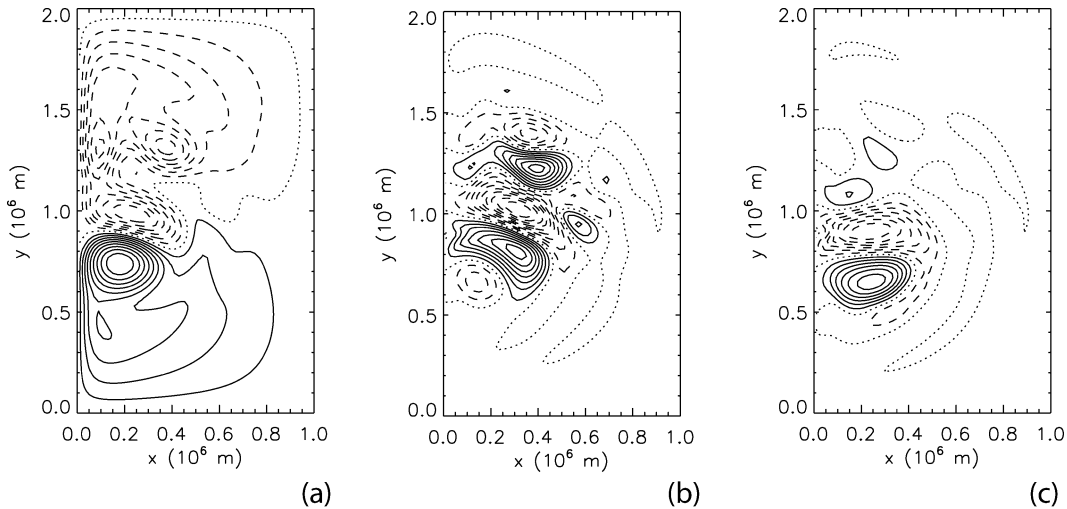
FIG. 6. As in Fig. 3 but for H_3 at $\tau_0 = 9.8 \times 10^{-2}$ Pa in the model with $\mathcal{F}_E$. The mode has a period of $\mathcal{P}_3 = 10.8$ yr.

jet, which would shift the jet northward (if this mode was superposed on the underlying steady state). Generally, the largest amplitudes occur in the center of the subpolar gyre, instead of near the separated jet.

To determine whether the modes destabilizing at H_3 are related, we introduce a "homotopy" parameter c_f and write the parameterization of the friction as follows:

$$\mathcal{F}(\mathbf{u}, h) = \mathcal{F}_M(\mathbf{u}, h) + \frac{c_f}{h}\nabla h \cdot \nabla \mathbf{u}. \quad (7)$$

When $c_f = 0$, the case $\mathcal{F}_M$ is obtained, whereas for $c_f = 1$ we obtain $\mathcal{F} = \mathcal{F}_E$. Of course, c_f can obtain any value between one and zero, which allows us to make a continuous transition from parameterization $\mathcal{F}_E$ to $\mathcal{F}_M$.

Starting at $c_f = 1$, first the steady state, the period and growth factor of the oscillatory mode are followed in c_f for constant τ_0 (Fig. 7a). The triangular markers in Fig. 7a indicate H_3 for both parameterizations of the

friction and the small dots show the positions where steady states and their stability have been computed. With decreasing c_f the low-frequency oscillatory mode smoothly becomes stable because $\sigma_r < 0$, while the period hardly changes (Fig. 7b). Hence, changing the parameterization of the friction from $\mathcal{F}_E$ to $\mathcal{F}_M$ stabilizes the low-frequency gyre mode.

For $c_f = 0$, τ_0 is increased and, although the mode first stabilizes, its growth rate increases suddenly in a relatively small interval near $\tau_0 = 1.3 \times 10^{-1}$ Pa. This can be seen by the relatively large amount of small dots in Fig. 7a, which are well spread in Fig. 7b. The fact that the same mode can be followed along a continuous path between both parameterizations indicates that the destabilizing mechanism is the same. However, the properties of the steady states differ for both parameterizations and hence also the location of the Hopf bifurcation.
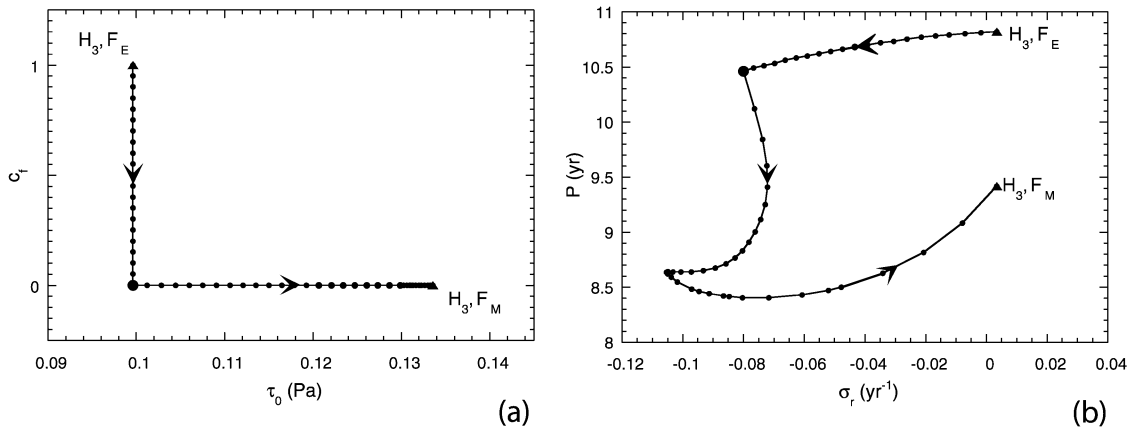
FIG. 7. (a) Schematic diagram of the path from the third Hopf bifurcation H_3 in the case with $\mathcal{F}_E$ to the third Hopf bifurcation in the case with $\mathcal{F}_M$. (b) Period of the low-frequency oscillatory mode against its growth rate along the path indicated in (a). The triangular markers indicate the Hopf bifurcations; the large dot indicates the change in continuation parameter from c_f to τ_0, and the small dots indicate the locations at which steady states and their stability have been computed.

b. Weakly nonlinear transient flows

In this section it will be demonstrated that the time-mean states and variability of time-dependent solutions in the weakly nonlinear parameter regime are consistent with the results from the bifurcation analyses in the previous section. Therefore, we have performed transient flow computations with all three of the parameterizations $\mathcal{F}_M$, $\mathcal{F}_E$, and $\mathcal{F}_F$ at relatively low forcing. As an initial state for these calculations, we have either used the state of rest, a final solution of a previous integration with a slightly different amplitude of the wind stress forcing, or one of the steady-state solutions calculated in the previous section.

The (time mean) minimum layer thickness $\overline{h}_{\min}$ for the equilibrated solutions are shown as markers in Fig. 8. Squares indicate states in which the flows have reached a steady state, while the circles indicate flows that remain time dependent. Filled circles indicate regular states (e.g., periodic and quasiperiodic flows) and open circles indicate irregular transient states. In the latter case, $\overline{h}_{\min}$ is calculated for the time-mean solution and its (equilibrium) range is indicated by an "error bar." In Figs. 8a and 8b, the steady-state branches, calculated in the previous section, have been added for comparison.

In the case with $\mathcal{F}_M$ (Fig. 8a), the steady solutions calculated for the time-dependent flow are in close agreement with that of the jet-down branch computed with the steady-state solver. The first sign of time dependence occurs at $\tau_0 = 8.5 \times 10^{-2}$ Pa, where a periodic orbit appears with a period of $\mathcal{P} = 1.8$ yr. The value of τ_0, the period, and pattern of the variability show that this is the periodic orbit arising from H_2 (Fig. 2a).

The time-mean minimum layer thicknesses $\overline{h}_{\min}$ of the transient flow calculations with $\mathcal{F}_E$ also closely agree with those of the underlying bifurcation diagram (Fig. 8b). The steady solutions that have been found correspond to those on both the jet-down as well as on the jet-up branch. The solutions near the jet-up branch become time dependent at $\tau_0 = 6.8 \times 10^{-2}$ Pa, which agrees nicely with the destabilization of the steady jet-up solution by the gyre mode at the Hopf bifurcation H_1. Also the dominant period of $\mathcal{P} = 18.5$ yr corresponds to the period of this internal oscillatory gyre mode. The solutions that follow the jet-down branch first show time-dependent behavior after the Hopf bifurcation H_2. It is not surprising that the dominant period is again $\mathcal{P} = 1.8$ yr, which clearly relates this behavior to the oscillatory mode that destabilizes at this Hopf bifurcation. Hence, there is an overall agreement between the bifurcation diagrams calculated in the previous sections and the transient flow computations presented here.

The bifurcation diagram for $\mathcal{F}_F$ has not been recomputed in this study since it is documented in Speich et al. (1995). However, it is clear from Fig. 8c that time-dependent solutions at higher forcing are near the jet-up branch, similar to the case $\mathcal{F}_E$. The solutions become

time dependent at $\tau_0 = 7.3 \times 10^{-2}$ Pa and the orbit has a dominant period of $\mathcal{P} = 10.5$ yr.

We expect that the effect of the parameterization of the lateral friction on the time-mean solutions is clearest in the parameter range where the bifurcation diagrams of $\mathcal{F}_M$ and $\mathcal{F}_E$ differ the most. This is for $6.0 \times 10^{-2} < \tau_0 < 9.0 \times 10^{-2}$ Pa, which is a relatively weak forcing.
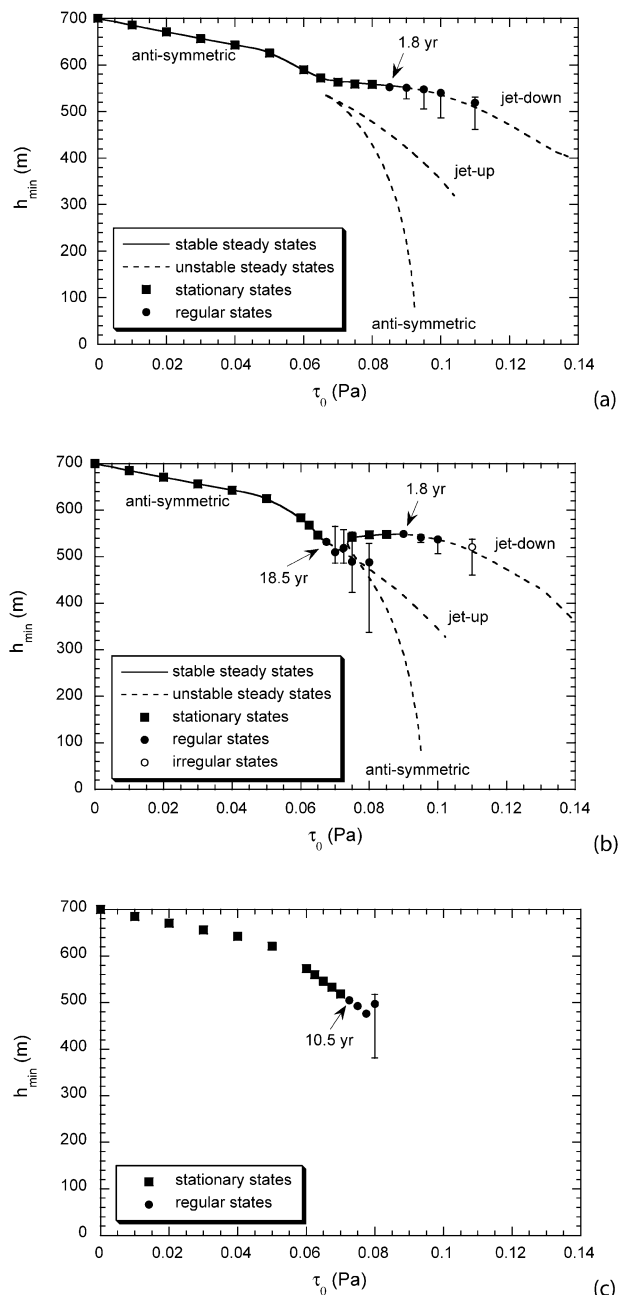
Fig. 8. The markers show the minimum layer thickness of the time-mean flow $\overline{h}_{\min}$ at different values of the wind stress forcing τ_0; the bars indicate the range in the minimum layer thickness $h_{\min}$ of the flow in statistical equilibrium. The results of the model (a) with $\mathcal{F}_M$, (b) with $\mathcal{F}_E$, and (c) with $\mathcal{F}_F$. In the cases with $\mathcal{F}_M$ and $\mathcal{F}_E$ the bifurcation structure of Fig. 2 is plotted as well.
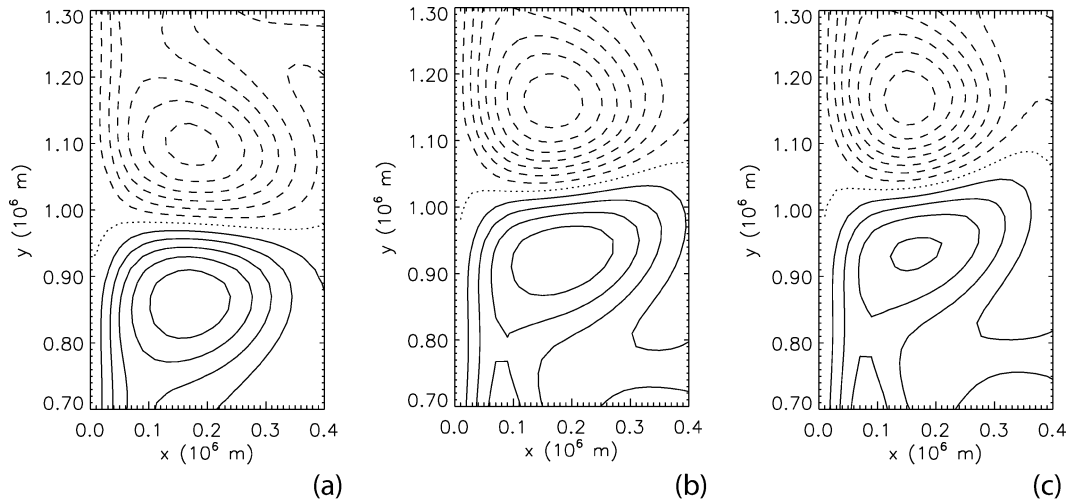
FIG. 9. Pattern of the layer thicknesses (contour interval is 20 m) for the stationary solutions at $\tau_0 = 6.5 \times 10^{-2}$ Pa for the cases with (a) $\mathcal{F}_M$, (b) $\mathcal{F}_E$, and (c) $\mathcal{F}_F$. Shown is a blowup of the area near the midaxis of the basin.

A blowup of the patterns of the steady layer thickness, h, near the midaxis of the basin is shown in Fig. 9 at $\tau_0 = 6.5 \times 10^{-2}$ Pa. After sufficient time integration, an almost antisymmetric stationary solution, which resembles a jet-down solution, is obtained for $\mathcal{F}_M$ (Fig. 9a). This is in contrast with the more pronounced stationary asymmetric jet-up solutions, which have been obtained in the other two cases (Figs. 9b,c). This clearly demonstrates that, in this wind stress regime, the solution is highly sensitive to the parameterization of the lateral friction, as was also indicated by the underlying bifurcation structure.

c. Low-frequency variability at large forcing

In order to investigate the impact of the different frictional parameterizations $\mathcal{F}_M$, $\mathcal{F}_E$, and $\mathcal{F}_F$ on the low-frequency variability of the flow in the strongly nonlinear regime, several 60-yr time integrations have been performed at realistic values of the wind stress forcing (although not at realistic viscosity). The time series of the basin-integrated kinetic energy are plotted in Figs. 10a,c for the frictional forms $\mathcal{F}_M$ and $\mathcal{F}_E$ at $\tau_0 = 1.1 \times 10^{-1}$ Pa. The Fourier spectrum (Fig. 10b) of the $\mathcal{F}_M$ time series indicates that the flow is slightly irregular, but has a pronounced low-frequency signal at a period of $\mathcal{P} = 8.9$ yr. For the same value of τ_0, the time series of the basin-averaged kinetic energy for the model with $\mathcal{F}_E$ (Fig. 10c) has much larger amplitudes (and also seems to be even less regular) than the time series for $\mathcal{F}_M$ (Fig. 10a). The Fourier spectrum for the $\mathcal{F}_E$ case in Fig. 10d shows an increase in energy at the low-frequency end.

The second peak in both cases, having a period of $\mathcal{P} = 1.9$ yr, can be related to the Rossby basin mode, which has a positive growth rate at this value of the wind stress forcing. The low-frequency gyre mode also has a positive growth rate in the case with $\mathcal{F}_E$ and can therefore

explain the decadal peak in Fig. 10d. On the contrary, in the case with $\mathcal{F}_M$ this gyre mode is still slightly damped. However, the steady state (in both cases) has already been destabilized by the Rossby basin mode and the flow has become time dependent, which will also influence the stability. Apparently, the gyre mode has destabilized prematurely in the presence of the Rossby basin mode oscillation in the case with $\mathcal{F}_M$. This has also been found in a two-layer shallow-water model (Nauw and Dijkstra 2001) and in a barotropic quasigeostrophic model (Van der Vaart et al. 2002). In the latter study, the mechanism of the destabilization of a time-dependent solution, containing variability related to the presence of Rossby basin modes, by the low-frequency gyre mode is investigated. There, it is demonstrated to be similar to the destabilization of a steady state by the gyre mode. The difference in the linear stability properties of the steady states hence very well explains the much larger low-frequency power in the case $\mathcal{F}_E$.

Differences in temporal behavior also exist between the time-dependent solutions with $\mathcal{F}_E$ and $\mathcal{F}_F$, even at relatively small values of τ_0. In Fig. 11a, the time series of the kinetic energy of the time-dependent flow at $\tau_0 = 8.0 \times 10^{-2}$ Pa with $\mathcal{F}_E$ show large variations in $h_{\min}$. The signature of the excursions in this relaxation-type oscillation can also be seen in the error bars in Fig. 8b. The mean state has the jet displaced northward, since $h_{\min}$ is located near the jet-up branch, and the period of this oscillation is $\mathcal{P} = 18.5$ yr, comparable to the period of $\mathcal{P}_1 = 17.7$ yr of the gyre mode, which destabilizes at H_1. For $\mathcal{F}_F$ the same type of relaxation oscillation is found at this value of τ_0 (Fig. 11b), but the period is reduced to $\mathcal{P} = 9.0$ yr. The relation between the low-frequency gyre modes, the limit cycles formed at slightly supercritical conditions, and the evolution into large-amplitude relaxation oscillations with a characteristic
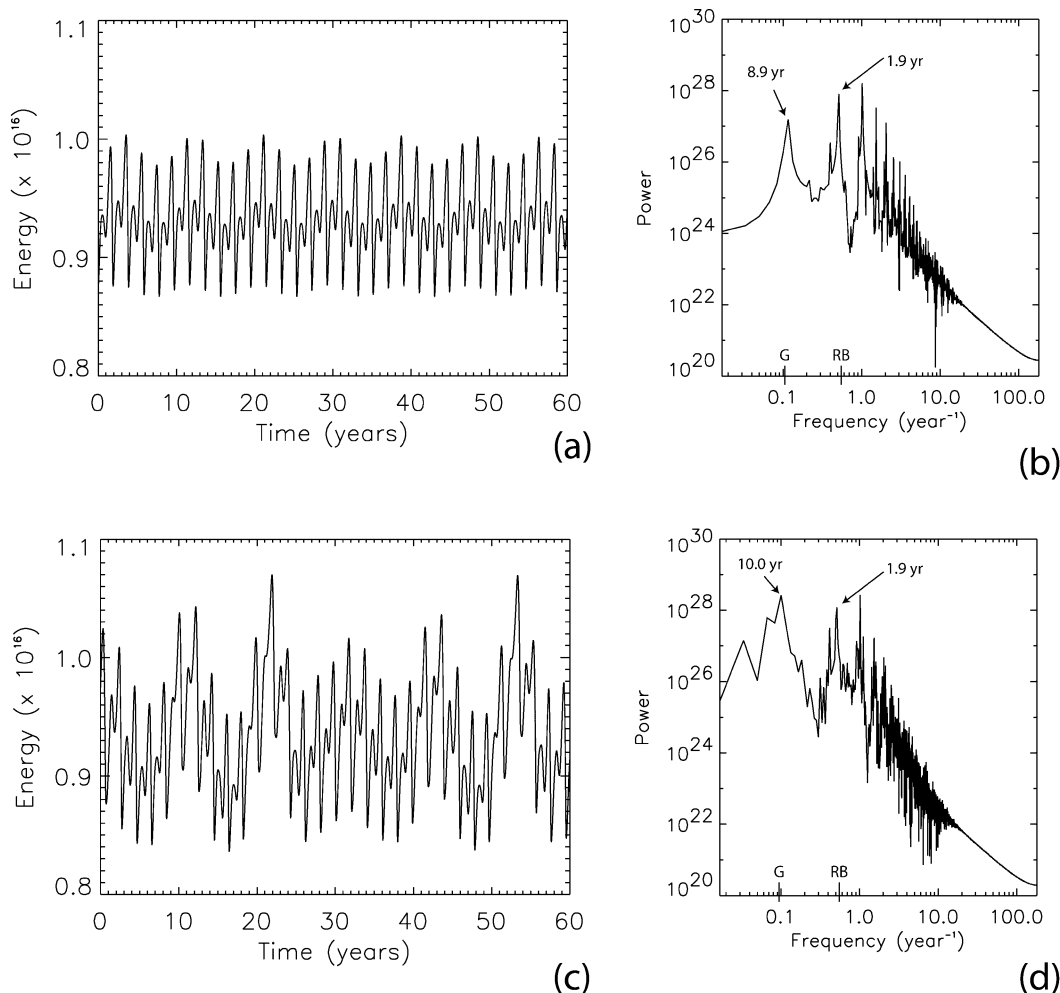
FIG. 10. Time series of the (left) kinetic energy and (right) their Fourier spectra at $\tau_0 = 1.1 \times 10^{-1}$ Pa (on the jet-down branch). (top) The case with $\mathcal{F}_M$, and (bottom) the case with $\mathcal{F}_E$. The frequencies of the gyre mode and the Rossby basin mode at criticality are indicated on the horizontal axis of the Fourier spectra in the panels on the right-hand side.

slow growth and quick destruction of the recirculation gyres have been extensively studied in Chang et al. (2001). The differences in stability properties and the sensitivity of the period of the gyre mode must be responsible for the different behavior. The sensitivity of the period of the gyre mode is related to its existence through a merging of two stationary modes (Simonnet and Dijkstra 2002). At the point of merging the two modes have the same (negative) growth rate and zero frequency and form an oscillatory pair. As the wind stress forcing is increased, the asymmetry of the steady state solution increases. Through the latter, the growth rate and frequency will also increase, thereby decreasing the period in a small range of parameters from infinity to decadal.

As mentioned in the introduction, the form $\mathcal{F}_E$ has been introduced because one is able to prove rigorously that the basin-integrated dissipation is a negative definite quantity. However, that one cannot demonstrate this property analytically for the other two frictional forms

does not mean that the dissipation is not consistently negative. The kinetic energy density of the shallow-water equations is $(\rho_0 h/2)\mathbf{u} \cdot \mathbf{u}$, and so the kinetic energy balance is obtained by adding the scalar product of $\rho_0 hu$ and (4a) to the scalar product of $\rho_0 hv$ and (4b) and to the scalar product of $(\rho_0/2)\mathbf{u} \cdot \mathbf{u}$ and (4c). After integrating this sum over the basin, one obtains

$$\frac{\partial}{\partial t}(\langle \mathcal{K} \rangle + \langle \mathcal{P} \rangle) = \langle \mathcal{D} \rangle + \langle \mathcal{W} \rangle, \qquad (8a)$$

where

$$\mathcal{K} = \frac{1}{2}\rho_0 h(u^2 + v^2), \qquad (8b)$$

$$\mathcal{P} = \frac{1}{2}\rho_0 g' h^2, \qquad (8c)$$

$$\mathcal{D} = A_H \rho_0 [uh\mathcal{F}^x(u, h) + vh\mathcal{F}^y(v, h)], \qquad (8d)$$

$$\mathcal{W} = u\tau^x, \qquad (8e)$$

and angle brackets indicate basin integration. In the equation above, $\langle \mathcal{K} \rangle$ and $\langle \mathcal{P} \rangle$ represent the basin-integrated kinetic and potential energy. The time derivative of their sum balances the input of kinetic energy through the wind stress $\langle \mathcal{W} \rangle$ and the dissipation $\langle \mathcal{D} \rangle$.

The time series of the terms $\partial \langle \mathcal{K} \rangle / \partial t$, $\partial \langle \mathcal{P} \rangle / \partial t$, $\langle \mathcal{W} \rangle$, and $-\langle \mathcal{D} \rangle$ are plotted for the case at $\tau_0 = 1.1 \times 10^{-1}$ Pa for $\mathcal{F}_M$ in Fig. 12a, and their time-averaged values are given in the first row of Table 3. On the average, the wind input, $\langle \mathcal{W} \rangle$ (heavy dashed), and the negative of the dissipation, $-\langle \mathcal{D} \rangle$ (heavy solid), balance, and over the whole integration time the dissipation $\langle \mathcal{D} \rangle$ is always a consistently negative quantity. The changes in kinetic (light dashed) and potential energy (light solid) are much smaller, and tendencies in the potential energy are correlated with the dissipation. This behavior is qualitatively the same for the case $\mathcal{F}_E$ (see Fig. 12b and the second column of Table 3). The results for the cases $\mathcal{F}_E$ (Fig. 12c) and $\mathcal{F}_F$ (Fig. 12d) at $\tau_0 = 8.0 \times 10^{-2}$ Pa also indicate that the dissipation is a consistently negative quantity for $\mathcal{F}_F$. These relaxation oscillations also indicate a similar correlation between tendencies in the potential energy and dissipation as seen in Figs. 12a and 12b.

d. The physics of the frictional asymmetries

In sections 3b and 3c, it has been shown that the different frictional forms lead to differences in the steady-state solutions, stability properties, and subsequent temporal variability. However, it remains difficult to trace the precise physics responsible for these differences using only the results of the double-gyre 1.5-layer shallow-water model. The bifurcation diagrams in Fig. 2 show that the different connections of the imperfect pitchfork bifurcation already have their origins in the low-forcing regime, just before the appearance of multiple equilibria. Here, already differences occur between steady-state solutions and between the terms in the momentum equations in (4a) and (4b). These differences are primarily located in the area of the separated jet, but also in area of the recirculation gyres (not shown). Hence, as a first attempt to explain the effect of the parameterization on the position of the separated jet one may possibly neglect the inertial terms in the 1.5-layer shallow-water model. A priori, we know that this will not provide the answer to the physics behind the specific connection of the branches because the (imperfect) pitchfork bifurcations exist by the grace of the nonlinear inertial terms. Moreover, the effect of neglecting the inertial terms on the double-gyre circulation and in particular the position of its separated jet will be discussed at the end of this section.

Without the inertial terms, however, the problem remains nonlinear and analytical solutions cannot easily be obtained. These nonlinearities are associated with the layer thickness field h, and therefore one can expect that they will be greatest in the area of the midlatitude jet.

This suggests that the effect of the parameterization of the friction may be understood by considering simple parallel zonal flows in a channel. We define the channel's width as $2L_c$, the velocity field as $u = u(y)$ and $v = 0$, and the layer thickness field as $h = h(y)$.

With these approximations, the 1.5-layer shallow-water model equations in (4a) and (4b) reduce to

$$0 = A_H \mathcal{F}^x(u, h) + \frac{\tau^x(y)}{\rho_0 h} \quad \text{and} \quad (9a)$$

$$(f_0 + \beta_0 y)u = -g' \frac{dh}{dy}, \quad (9b)$$

while (4c) is identically zero. The frictional terms become

$$\mathcal{F}_M^x(u, h) = \frac{d^2 u}{dy^2}, \quad (10a)$$

$$\mathcal{F}_E^x(u, h) = \frac{1}{h} \frac{d}{dy}\left(h \frac{du}{dy}\right), \quad \text{and} \quad (10b)$$

$$\mathcal{F}_F^x(u, h) = \frac{1}{h} \frac{d^2(uh)}{dy^2}, \quad (10c)$$

with no-slip boundary conditions at the channel walls

$$y = \pm L_c : u = 0. \quad (11)$$

To ensure overall mass conservation, an integral condition for the layer thickness must be enforced; that is,

$$\frac{1}{2L_c} \int_{-L_c}^{L_c} h(y) \, dy = H_0. \quad (12)$$

Steady states of these equations were determined for an idealized pure easterly wind stress forcing $\tau^x(y) = \tau_0$ in a channel of width $2L_c = 200$ km by the software package AUTO (Doedel 1981). In Fig. 13a, the bifurcation diagrams are shown for the three different frictional forms. In this diagram, the maximum value of the zonal velocity, u_{max}, is plotted versus the wind stress strength τ_0; the parameters β_0, f_0, g', ρ_0 are the same as in Table 1, while slightly different values are used for $H_0 = 1.0 \times 10^3$ m and $A_H = 5.0 \times 10^2$ m^2 s^{-1}. For $\tau_0 < 1.3 \times 10^{-1}$ Pa, the bifurcation diagrams are very similar for each type of friction. For larger values of τ_0, the curves for $\mathcal{F}_M$ and $\mathcal{F}_E$ undergo a saddle-node bifurcation and, at the end point of the curve, the layer thickness becomes zero. The curve for $\mathcal{F}_M$ does not undergo a saddle-node bifurcation, but also ends at a solution with outcropping.

The solutions for the zonal velocity and layer thickness at $\tau_0 = 1.0 \times 10^{-1}$ Pa (indicated by the marker in Fig. 13a) are plotted in Fig. 13b for each form of the friction. While all velocity profiles have the jet axis slightly shifted northward with respect to the center of the channel, this effect is weakest for the frictional form $\mathcal{F}_M$. The maxima of the zonal velocity are positioned at $y_M = 0.7 \times 10^4$ m, $y_E = 1.6 \times 10^4$ m, and $y_F = 2.9$
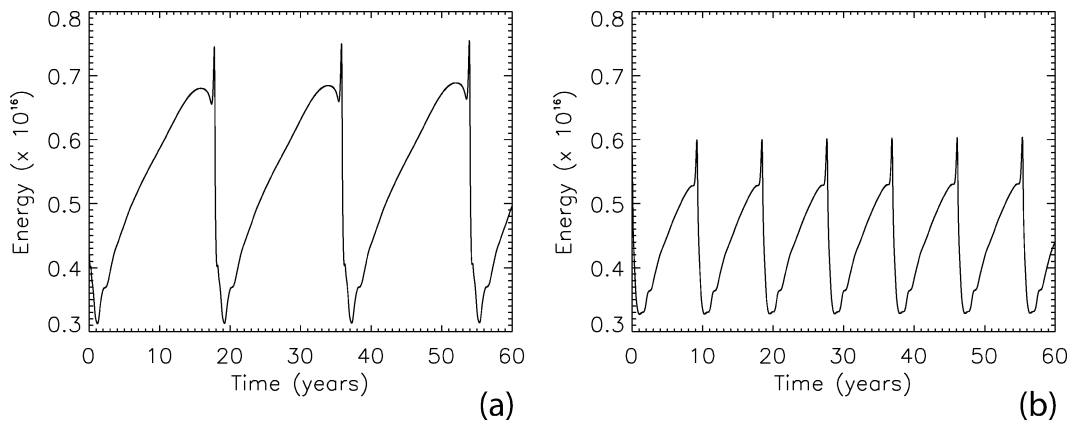
FIG. 11. Time series of the kinetic energy of the time-dependent flows at $\tau_0 = 8.0 \times 10^{-2}$ Pa (on the jet-up branch). (left) The case with $\mathcal{F}_E$ and (right) the case with $\mathcal{F}_F$.
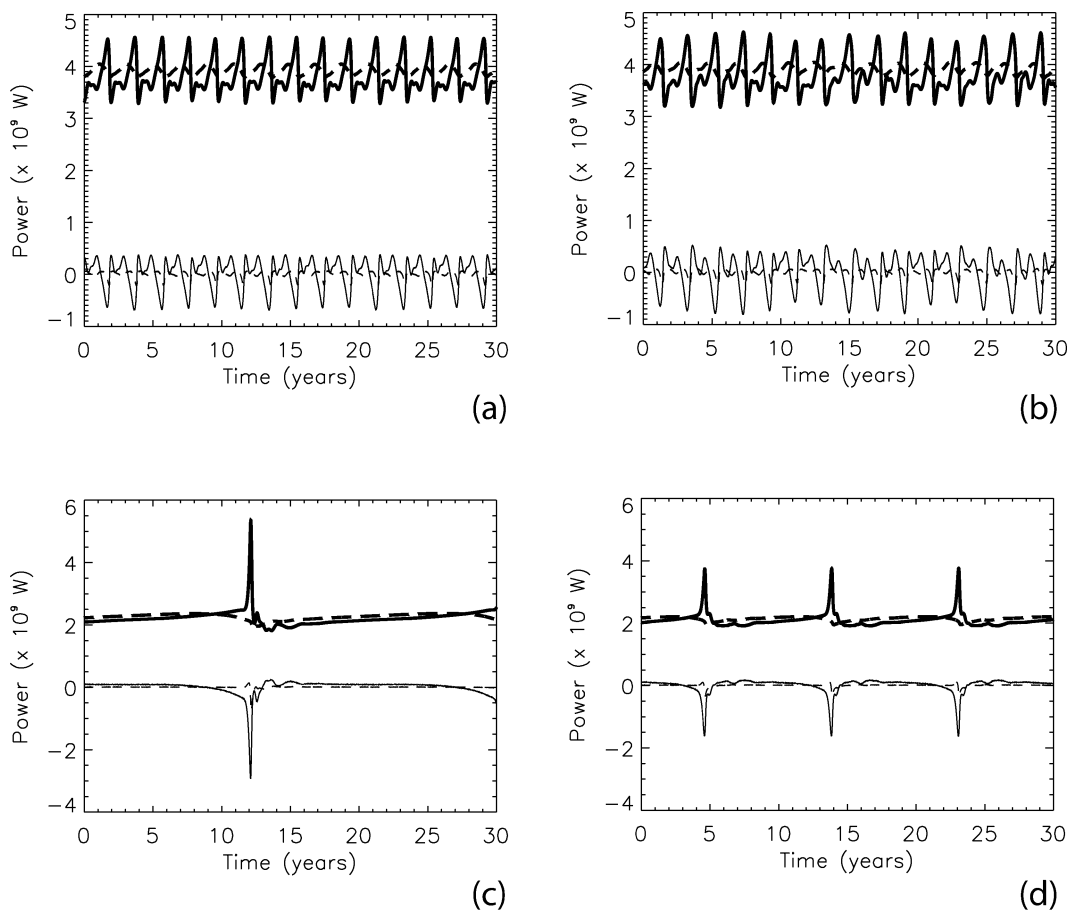
FIG. 12. Time series of terms in the energy equation (8). Plotted are the negative of the dissipation, $-\langle \mathcal{D} \rangle$ (heavy solid), the energy input by the wind, $\langle \mathcal{W} \rangle$ (heavy dashed), and the time derivatives of the potential $\langle \partial \mathcal{P}/\partial t \rangle$ (light solid) and kinetic energy $\langle \partial \mathcal{K}/\partial t \rangle$ (light dashed). The cases with (a) $\mathcal{F}_M$ and (b) $\mathcal{F}_E$ at $\tau_0 = 1.1 \times 10^{-1}$ Pa (on the jet-down branch) and the cases with (c) $\mathcal{F}_E$ and (d) $\mathcal{F}_F$ for the time-dependent solutions at $\tau_0 = 8.0 \times 10^{-2}$ Pa (on the jet-up branch).

TABLE 3. Time-averaged values of the terms in (8) for the cases shown in Fig. 12.

	$-\langle \mathcal{D} \rangle$	$\langle \mathcal{W} \rangle$	$\langle \partial \mathcal{K}/\partial t \rangle$	$\langle \partial \mathcal{P}/\partial t \rangle$
$\mathcal{F}_M$ ($\tau_0 = 1.1 \times 10^{-1}$ Pa)	3.8×10^9	3.9×10^9	3.5×10^6	7.9×10^5
$\mathcal{F}_E$ ($\tau_0 = 1.1 \times 10^{-1}$ Pa)	3.8×10^9	3.9×10^9	-1.4×10^6	-3.0×10^5
$\mathcal{F}_E$ ($\tau_0 = 8.0 \times 10^{-2}$ Pa)	2.2×10^9	2.3×10^9	9.2×10^6	1.9×10^6
$\mathcal{F}_F$ ($\tau_0 = 8.0 \times 10^{-2}$ Pa)	2.1×10^9	2.1×10^9	7.4×10^6	6.9×10^5

$\times \ 10^4$ m. Correspondingly, the layer thickness structure of $\mathcal{F}_M$ is the least asymmetric and that of $\mathcal{F}_F$ is the most asymmetric. Hence, the solutions of this simple model indeed show a stronger jet-up preference for the types of friction $\mathcal{F}_E$ and $\mathcal{F}_F$.

One can explain these results in a bit more detail by going back to the interpretation of the components of the stress tensor. In this simple model, only the flux of zonal momentum in the meridional direction is relevant. For the frictional form $\mathcal{F}_M$, we can rewrite (9a) as

$$\frac{d}{dy}\left(A_H \frac{du}{dy}\right) = -\frac{\tau^x(y)}{\rho_0 h}, \tag{13}$$

whereas for $\mathcal{F}_E$, we can write (9a) as

$$\frac{1}{H_0}\frac{d}{dy}\left(h \times A_H \frac{du}{dy}\right) = -\frac{\tau^x(y)}{\rho_0 H_0}, \tag{14}$$

where the factor H_0 has been included to have an identity between two fluxes of zonal momentum. Because of (9b), an eastward jet is always associated with a negative gradient of the layer thickness and hence h is smaller (larger) north (south) of the midaxis of the channel. For a wind stress that is symmetrical around the midaxis of the channel, $\tau^x(y) = \tau^x(-y)$ [which is true for the special case with a constant wind stress, $\tau^x(y) = \tau_0$], the parameterizations can clearly be distinguished. In (13), the mixing coefficient A_H in the stress tensor is constant and therefore symmetrical. The wind stress, however, is acting on a thinner (thicker) layer in the north (south) that causes the momentum input to be asymmetrical. The opposite holds for (14), where the momentum input

is symmetrical while the mixing coefficient is layer dependent, that is, stronger (weaker) in the south (north). Stronger forcing or weaker mixing north of the midaxis of the basin both cause the jet to be displaced northward. However, the results in Fig. 13 show that a variable mixing coefficient has a stronger asymmetric effect than variable forcing.

One can also consider this in another way. Suppose we prescribe a symmetric velocity profile and a purely antisymmetric thermocline profile and ask: what wind stress shape is needed to force this as a steady flow in the channel? In the simplest case, neglecting the β effect, we choose

$$h(y) = H_0\left[1 - \frac{1}{4}\sin\left(\frac{\pi y}{2L_c}\right)\right] \quad \text{and} \tag{15a}$$

$$u(y) = U_0 \cos\left(\frac{\pi y}{2L_c}\right) \tag{15b}$$

with $U_0 = \pi g' H_0/(8f_0 L_c)$. For this flow field, the general solution for the wind stress profile with each of the frictional parameterizations is

$$\tau^x(y) = \tau_0\left[\cos\left(\frac{\pi y}{2L_c}\right) - A_{as}\sin\left(\frac{\pi y}{L_c}\right)\right], \tag{16}$$

where $\tau_0 = \rho_0 H_0 A_H U_0 \pi^2/(4L_c^2)$ and A_{as} is a constant that determines the degree of asymmetry in the wind stress forcing. In quasigeostrophic theory, $A_{as} = 0$, but with $\mathcal{F}_M$, $\mathcal{F}_E$, and $\mathcal{F}_F$ in shallow-water models, one finds $A_{as} = 1/8$, $A_{as} = 1/4$, and $A_{as} = 1/2$, respectively. Hence, the asymmetry needed in the wind stress forcing to
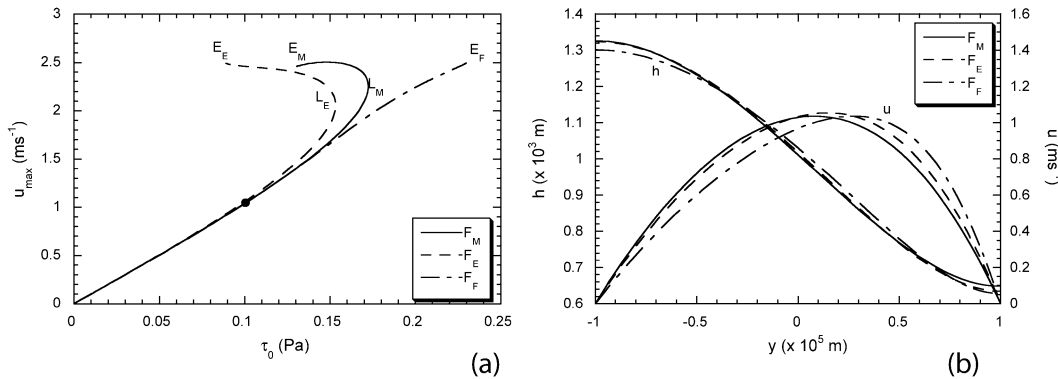
FIG. 13. (a) Bifurcation diagrams showing the maximum (zonal) velocity in a channel, u_{max}, for each type of friction vs the wind stress strength τ_0. (b) Zonal velocity u and layer thickness h for $\tau_0 = 1.0 \times 10^{-1}$ Pa for each type of friction, with $\mathcal{F}_M$ (solid), $\mathcal{F}_E$ (dashed), and $\mathcal{F}_F$ (dashed–dotted).
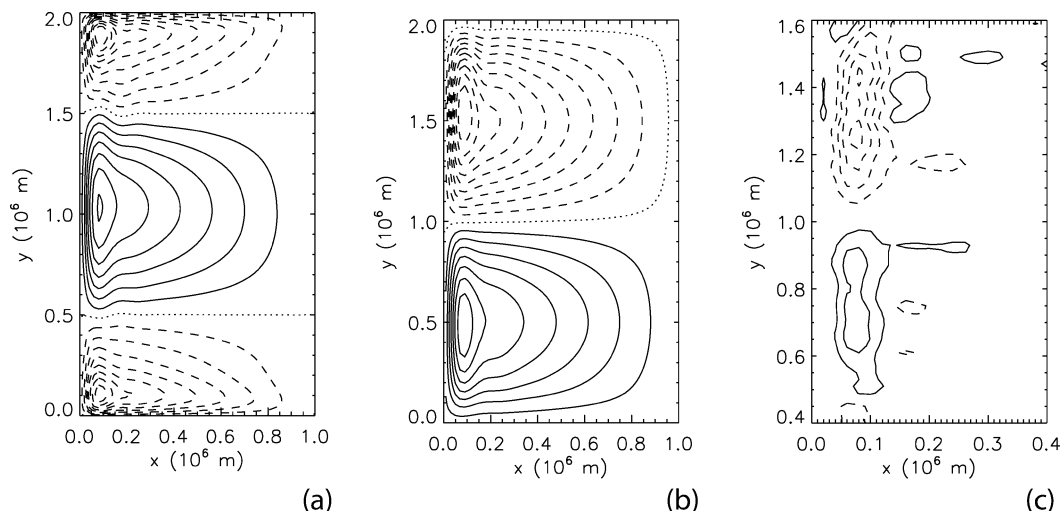
FIG. 14. Contours of (a) the zonal velocity u and (b) the layer thickness h at $\tau_0 = 8.0 \times 10^{-2}$ Pa for the case with $\mathcal{F}_M$ without inertia. (c) Blowup in the separation area of the difference in zonal velocity, $u_M - u_E$, between the cases with $\mathcal{F}_M$ and $\mathcal{F}_E$.

maintain a symmetric flow is highly dependent on the parameterization of the friction.

e. The effect of inertia

While the discussion of the flow in a channel provides an explanation for the different northward displacements of the jet for each of the frictional forms, with $\mathcal{F}_M$ having the smallest northward displacement, it does not, however, explain the preference for solutions with a southward displacement of the jet in the double-gyre circulation, as found for $\mathcal{F}_M$ (Fig. 9a). The displacement is most likely accomplished by inertia, which may cause an opposing effect to the asymmetries introduced by the frictional forms. The effect of inertia is demonstrated in the full model, where it has been neglected in a time integration at $\tau_0 = 8.0 \times 10^{-2}$ Pa for the cases with $\mathcal{F}_M$ and $\mathcal{F}_E$. In the steady solution for $\mathcal{F}_M$ the maximum zonal velocity is found north of the midaxis of the basin (Fig. 14a). The pattern of the layer thickness now shows a broad jet (Fig. 14b) because the recirculation gyres have vanished (Fig. 14b). From a blowup of the difference in zonal velocity between the two cases, $u_M - u_E$ (Fig. 14c), one observes that the maximum zonal velocity in the case with $\mathcal{F}_E$ is even slightly more shifted to the north compared to the case with $\mathcal{F}_M$. This confirms the results of the simple model of a zonal flow in a channel. Moreover, one can deduce that there exists a competition between a northward displacement of the separated jet by the friction and a southward displacement by the nonlinear advection. The presence of nonlinear advection will introduce multiple equilibria, thereby introducing both a jet-up and a jet-down solution. However, in the parametric regime with a single solution, where advection only has a minor importance, the parameter-

ization of the friction will essentially determine the type of solution.

4. Discussion

It has been known for some time that the separation behavior of western boundary currents, such as the Gulf Stream, in many ocean models is sensitive to the details of parameterization of subgrid-scale mixing processes of momentum (McWilliams 1996; Chassignet and Garraffo 2001). The precise physics of this sensitivity has so far been unclear due to the difficulty of the multiscale, multiprocess representation in these ocean models. By tackling a puzzling result in the bifurcation structure of shallow-water models, one possible reason for this sensitivity has been identified.

The qualitative differences between the imperfect pitchfork bifurcation found in shallow-water models of the double-gyre circulation (Jiang et al. 1995; Speich et al. 1995; Dijkstra and Molemaker 1999; Nauw and Dijkstra 2001; and this study) have their origin in frictionally induced asymmetries. Moreover, the parameterization of the friction influences the stability of the internal oscillatory modes. In these models, the parameterization of subgrid-scale mixing processes leads to differences in the time-averaged north–south jet displacement, even at weak wind stress forcing. The different stability properties of the internal modes is at the basis of differences in low-frequency variability in time-dependent flows at realistic forcing.

The reflection through the midaxis of the basin can be represented as the transformation

$$u \to u, \ v \to -v, \ y \to B/2 - y, \text{ and } h \to -h. \quad (17)$$

When the frictionless, unforced shallow-water equations

are considered on the f plane without inertia, then they are invariant with respect to this transformation (similar to the quasigeostrophic limit). When inertia is added, the reflection symmetry is broken in the momentum equations, but the continuity equation remains invariant. This is reflected in the different potential vorticity for quasigeostrophic and shallow-water equations. The latter is given by

$$\Pi = \frac{\zeta + f}{h} \qquad (18)$$

and is clearly asymmetric because of the dependence on the layer thickness. Hence, the asymmetry arises from the momentum equations and, as soon as the asymmetries are present either through inertia, friction, or forcing, these may be modified through the continuity constraint.

With the help of an analytical model of the flow in a zonal channel, the precise physics of the asymmetries can be described. The solutions will differ between the case with asymmetry in the forcing and constant mixing coefficient and the case with a symmetric forcing and a layer thickness dependent mixing coefficient. The results can be summarized as "asymmetric mixing induces a stronger north–south asymmetry than asymmetric forcing." However, all of the parameterizations cause the separated jet to be displaced northward. Moreover, without the inertial terms, the double-gyre flow in both cases with $\mathcal{F}_M$ and $\mathcal{F}_E$ shows a stronger circulation in the subpolar gyre with the maximum zonal velocity in the jet north of the midaxis of the basin, similar to the Sverdrup regime solution in Chassignet and Gent (1991). In the weak wind stress forcing limit, inertia is not strong enough to oppose the effect of the friction in the cases $\mathcal{F}_E$ and $\mathcal{F}_F$, but it overcomes the effect of the friction in the case with $\mathcal{F}_M$. In the latter case, inertia causes a southward displacement of the jet. With stronger inertia (at large wind stress forcing), eventually a jet-down solution is also found for the frictional form $\mathcal{F}_E$ (Fig. 8b). Hence, the original assumption in Chassignet and Gent (1991), that asymmetry in the gyre strength is the main cause for a southward displacement once inertia and dissipation are included, is not justified. When both are included, a competition arises between the effect of friction and inertia, causing either a northward or a southward displacement of the jet.

What do these results imply for separation dynamics in ocean models? For very high resolution models the effect of inertia, in particular through the high degree of eddy activity, is probably so strong that the frictional effects will be of minor importance. However, when inertia is not that strong, for example during a spinup of these models or in ocean models of intermediate resolution, such as are used in climate models, the separation dynamics of western boundary currents will certainly be dependent on the parameterization of the friction. The results here suggest that one should be cautious in choosing the parameterization of lateral friction in layer models. While one is tempted to choose a priori negative definite dissipation schemes, such as generalizations of $\mathcal{F}_E$, the results here show that there will be qualitative differences in separation between solutions at intermediate and high resolution. Other schemes such as $\mathcal{F}_M$, which turn out to also give a consistently negative dissipation, will be less sensitive to the resolution and probably lead to a better separation.

REFERENCES

Böning, C. W., and R. G. Budich, 1992: Eddy dynamics in a primitive equation model: Sensitivity to horizontal resolution and friction. *J. Phys. Oceanogr.,* **22,** 361–381.

Cessi, P., 1991: Laminar separation of colliding western boundary currents. *J. Mar. Res.,* **49,** 697–717.

——, and G. R. Ierley, 1995: Symmetry-breaking multiple equilibria in quasigeostrophic, wind-driven flows. *J. Phys. Oceanogr.,* **25,** 1196–1205.

Chang, K.-I., M. Ghil, K. Ide, and C.-C. A. Lai, 2001: Transition to aperiodic variability in a wind-driven double-gyre circulation model. *J. Phys. Oceanogr.,* **31,** 1260–1286.

Chassignet, E., and P. Gent, 1991: The influence of boundary conditions on midlatitude jet separation in ocean models. *J. Phys. Oceanogr.,* **21,** 1290–1299.

——, and Z. D. Garraffo, 2001: Viscosity parameterization and the Gulf Stream separation. *From Stirring to Mixing in a Stratified Ocean: Proc. 'Aha Huliko'a Hawaiian Winter Workshop,* Honolulu, HI, University of Hawaii at Manoa, 37–41.

Dijkstra, H. A., 2000: *Nonlinear Physical Oceanography.* Kluwer Academic, 480 pp.

——, and C. A. Katsman, 1997: Temporal variability of the wind-driven quasi-geostrophic double gyre ocean circulation: Basic bifurcation diagrams. *Geophys. Astrophys. Fluid Dyn.,* **85,** 195–232.

——, and M. J. Molemaker, 1999: Imperfections of the North-Atlantic wind-driven ocean circulation: Continental geometry and wind stress shape. *J. Mar. Res.,* **57,** 1–28.

Doedel, E. J., 1981: AUTO: A program for the automatic bifurcation analysis of autonomous systems. *Proc. 10th Manitoba Conf. on Numerical Mathematics and Computing,* Winnipeg, MB, Canada, University of Manitoba, 265–284.

Gent, P. R., 1993: The energetically consistent shallow-water equations. *J. Atmos. Sci.,* **50,** 1323–1325.

Holland, W. R., and L. B. Lin, 1975: On the generation of mesoscale eddies and their contribution to the ocean general circulation. I. A preliminary numerical experiment. *J. Phys. Oceanogr.,* **5,** 642–657.

Hurlburt, H. E., and P. J. Hogan, 2000: Impact of 1/8° to 1/64° resolution on Gulf Stream model–data comparisons in basin-scale subtropical Atlantic Ocean models. *Dyn. Atmos. Oceans,* **32,** 283–329.

Jiang, S., F.-F. Jin, and M. Ghil, 1995: Multiple equilibria and ape-riodic solutions in a wind-driven double gyre, shallow water model. *J. Phys. Oceanogr.,* **25,** 764–786.

McWilliams, J. C., 1996: Modeling the ocean general circulation. *Annu. Rev. Fluid Mech.,* **28,** 215–248.

Munk, W., 1950: On the wind-driven ocean circulation. *J. Meteor.,* **7,** 79–93.

Nadiga, B. T., and B. P. Luce, 2001: Global bifurcation of Shilnikov type in a double-gyre ocean model. *J. Phys. Oceanogr.,* **31,** 2669–2690.

Nauw, J. J., and H. A. Dijkstra, 2001: The origin of low-frequency variability of double-gyre wind-driven flows. *J. Mar. Res.,* **59,** 567–597.

Pedlosky, J., 1987: *Geophysical Fluid Dynamics.* 2d ed. Springer-Verlag, 710 pp.

——, 1996: *Ocean Circulation Theory.* Springer, 453 pp.

Schmeits, M. J., and H. A. Dijkstra, 2000: Physics of the 9-month variability in the Gulf Stream region: Combining data and dy-namical systems analyses. *J. Phys. Oceanogr.,* **30,** 1967–1987.

——, and ——, 2001: Bimodal behavior of the Kuroshio and the Gulf Stream. *J. Phys. Oceanogr.,* **31,** 3435–3456.

Simonnet, E., and H. A. Dijkstra, 2002: Spontaneous generation of low-frequency modes of variability in the wind-driven ocean circulation. *J. Phys. Oceanogr.,* **32,** 1747–1762.

Smith, R. D., M. E. Maltrud, F. O. Bryan, and M. W. Hecht, 2000: Numerical simulation of the North Atlantic Ocean at 1/10°. *J. Phys. Oceanogr.,* **30,** 1532–1561.

Speich, S., H. A. Dijkstra, and M. Ghil, 1995: Successive bifurcations in a shallow-water model applied to the wind-driven ocean cir-culation. *Nonlinear Processes Geophys.,* **2,** 241–268.

Stommel, H., 1948: The westward intensification of wind-driven ocean currents. *Trans. Amer. Geophys. Union,* **29,** 202–206.

Sverdrup, H. U., 1947: Wind-driven currents in a baroclinic ocean with application to the equatorial current in the eastern Pacific. *Proc. Natl. Acad. Sci.,* **33,** 318–326.

Van der Vaart, P. C. F., H. M. Schuttelaars, D. Calvete, and H. A. Dijkstra, 2002: Instability of time-dependent wind-driven ocean gyres. *Phys. Fluids,* **14,** 3601–3615.